Zhao et al. *Zool. Res.* 2026, 47(6): 1926−1940
https://doi.org/10.24272/j.issn.2095-8137.2025.612
https://cstr.cn/32248.14.zr.2025.612

ZR | Zoological Research

Article Open Access

Spatial transcriptomics and N-glycoproteomics reveal breed-dependent immune and structural responses in *Mycoplasma hyopneumoniae*-infected pig lungs

Zhen-Jian Zhao[1,#], Jia-Miao Chen[1,#], Dong Chen[1], Sheng-Di Cui[1], Shi-Xin Yu[1], Qi Shen[1], Patrick Kofi Makafui Tecku[1], Run-Jie Huang[1], Yao-Xi Zhou[1], Ping-Xian Wu[2], Guo-Qing Tang[1,*]

[1] *State Key Laboratory of Swine and Poultry Breeding Industry*, *Key Laboratory of Agricultural Bioinformatics*, *Ministry of Education*, *Key Laboratory of Livestock and Poultry Multi-omics*, *Ministry of Agriculture and Rural Affairs and Farm Animal Germplasm Resources and Biotech Breeding Key Laboratory of Sichuan Province*, *College of Animal Science and Technology*, *Sichuan Agricultural University*, *Chengdu*, *Sichuan* 611130, *China*

[2] *Chongqing Academy of Animal Sciences*, *Chongqing* 402460, *China*

ABSTRACT

Mycoplasma hyopneumoniae (Mhp) is a major cause of enzootic pneumonia in pigs, yet the molecular and spatial determinants underlying breed-specific susceptibility remain incompletely understood. Here, we integrated spatial transcriptomics, quantitative proteomics, and N-glycoproteomics to compare lung responses to experimental Mhp infection in Chenghua pigs with higher susceptibility and Yorkshire pigs with relative resilience. Under an identical inoculation dose, Chenghua pigs exhibited more severe clinical and pathological manifestations than Yorkshire pigs, despite comparable pulmonary Mhp loads at this late stage of infection. This observation suggests that disease severity is associated with differences in host response organization rather than with overall pathogen burden. Spatial analyses revealed a shared spatial and cellular infection framework across breeds, with marked differences in regulatory balance. Across spatial clusters, Chenghua pigs exhibited coordinated activation of TNF-α-NF-κB and IL-6-JAK-STAT3 signaling, accompanied by relative attenuation of IFN-I responses. These inflammatory features co-occurred with hypoxia- and mTORC1-related metabolic reprogramming, activation of stress-response pathways, and engagement of tissue remodeling programs. Transcription factor analyses further indicated increased activity of *HIF1A, RELA* and *STAT3*, together with reduced *IRF9*/*STAT2*-associated regulatory activity. Immune deconvolution and multiplex immunofluorescence revealed enrichment of M0/M2 macrophages, plasma cells, and activated mast cells, alongside reduced M1 macrophage and $CD8^+$ T-cell signatures. These changes delineated inflammatory niches characterized by relatively high *IL1B* expression and enrichment of mast cells. Ligand–receptor analysis revealed enhanced BAFF/APRIL–B-cell signaling features and amplification of MHC-II, RESISTIN, and CXCL networks in Chenghua pigs. Proteomic and N-glycoproteomic profiling further revealed disruption of junctional and extracellular-matrix components, together with extensive breed-specific remodeling of barrier and antigen-presentation-related glycoproteins in Chenghua pigs. Together, these findings provide a spatially resolved description of breed-dependent differences in immune, metabolic, and structural responses observed during chronic Mhp infection.

Keywords: *Mycoplasma hyopneumoniae*; Swine enzootic pneumonia; Spatial transcriptomics; N-glycoproteomics; Breed-specific susceptibility

INTRODUCTION

Mycoplasma hyopneumoniae (Mhp) infection is one of the most important chronic respiratory diseases in modern pig production (Maes et al., 2018), leading to impaired growth and poor feed conversion (Maes et al., 1996), and increased

This is an open-access article distributed under the terms of the Creative Commons Attribution Non-Commercial License (http://creativecommons.org/licenses/by-nc/4.0/), which permits unrestricted non-commercial use, distribution, and reproduction in any medium, provided the original work is properly cited.

Copyright ©2026 Editorial Office of Zoological Research, Kunming Institute of Zoology, Chinese Academy of Sciences

Received: 06 February 2026; Accepted: 17 March 2026; Online: 18 March 2026

Foundation items: The study was supported by the Sichuan Science and Technology Program (2021ZDZX0008, 2020YFN0024, 2021YFYZ0030), Earmarked Fund for the China Agriculture Research System (CARS-35-01A), National Key R&D Program of China (2018YFD0501204), National Natural Science Foundation of China (C170102), Sichuan Innovation Team of Pig (sccxtd-2021-08), and National Center of Technology Innovation for Pigs (NCTIP-XD/B01)

[#]Authors contributed equally to this work

*Corresponding author, E-mail: tyq003@163.com

susceptibility to secondary bacterial and viral infections (Chae, 2016; Saade et al., 2020). Mhp achieves colonization by recognizing receptors on host cell surfaces through a family of adhesins, such as P97/P102, subsequently inducing pathological changes predominantly characterized by lymphocyte and macrophage infiltration (Leal Zimmer et al., 2020). Mhp pathogenesis involves combined epithelial injury and immune evasion. The pathogen induces oxidative stress (Mucha et al., 2020), LAMP-dependent apoptosis (Bai et al., 2014), necroptosis (Zhang et al., 2025), and disruption of ciliary function, mucin secretion, and tight junctions, thereby weakening the mucosal barrier and promoting spread into the lower airways (Wang et al., 2020). In parallel, Mhp binds complement factor H (Yu et al., 2020), rewires NOD1/NF-κB signaling (Liu et al., 2017), and activates the NLRP3 inflammasome (Zhang et al., 2023) to both impair effective clearance and sustain chronic, cytokine-mediated inflammation. Current inactivated vaccines and antimicrobial regimens can reduce clinical signs and lesion severity but do not prevent colonization or transmission (Maes et al., 2020, 2021), and long-term antibiotic use raises concerns about resistance and food safety (Collignon & McEwen, 2019). Against this background, genetic improvement for Mhp resistance has emerged as a sustainable control strategy (Ando et al., 2016; Shimazu et al., 2014), yet the molecular basis of host resistance remains incompletely understood.

Challenge experiments have consistently shown that pig breeds differ markedly in disease course and lung lesion severity after Mhp infection (Fang et al., 2015; Zhang et al., 2021). Chinese indigenous breeds such as Meishan and Jiangquhai tend to develop more extensive and persistent lung lesions under standardized challenge conditions, whereas commercial breeds often show milder, self-limiting disease (Ni et al., 2019; Zhou et al., 2025). A comparative genomic study has shown that Chinese indigenous pigs have undergone positive selection at multiple loci associated with reproduction, fat deposition, and meat quality. This suggests that their heightened susceptibility to Mhp is unlikely to result primarily from direct selection on immune traits, but may instead reflect indirect reshaping of immune-related genetic features under long-term breeding selection (Xu et al., 2020). In parallel, another study reported significant differences in basal immune status and the expression of immune-related genes between Chinese indigenous pigs and commercial breeds, indicating that host genetic background influences immune response patterns to infection (Yang et al., 2022). Chenghua pigs are a representative indigenous breed from southwestern China and share key genetic and production characteristics with other local breeds (Wang et al., 2024). Field investigations have further reported a high prevalence of Mhp infection in this breed. Together, these features support the use of Chenghua pigs as a suitable model for investigating the molecular basis of heightened susceptibility to Mhp.

Previous transcriptomic studies indicate that disease-resistant pigs rapidly upregulate interferon-stimulated genes and strengthen cytokine-receptor interactions after Mhp infection (Ni et al., 2019). Disease evolution, however, is governed by a multilayered network that integrates pathogen recognition, innate and adaptive immune regulation, metabolic reprogramming, and post-translational modifications. Among these, protein N-glycosylation is one of the most prevalent modifications (Lee et al., 2015) and plays important roles in pathogen recognition, immune cell adhesion and migration, and inflammatory signaling (Clough et al., 2024; Li et al., 2025). Mhp adhesins engage host surface glycans to establish colonization (Deutscher et al., 2010, 2012), while chronic inflammation broadly remodels epithelial and matrix glycosylation patterns (Reily et al., 2019; Vicente et al., 2023). Thus, glycosylation is a plausible but largely unexplored determinant of host susceptibility. The lung is a structurally complex organ with marked regional differences in cellular composition, perfusion and ventilation, and microenvironmental cues (Rosales et al., 2024). Conventional tissue homogenization obscures this intrinsic spatial heterogeneity and hampers our ability to dissect interactions among pathogens, epithelial cells, and infiltrating immune cells at the microenvironmental scale (Megas et al., 2025). Spatial transcriptomics and multi-omics technologies have recently revealed localized immune niches and region-specific lesion progression in lung cancer (De Zuani et al., 2024; Tagore et al., 2025), COVID-19 (Lee et al., 2025), and fibrotic lung disease (Mayr et al., 2024). Yet, comparable spatially resolved, multi-layer analyses are lacking for respiratory Mhp infections and breed-dependent susceptibility.

Building on these considerations, we integrated spatial transcriptomics, quantitative proteomics, and N-glycoproteomics to systematically compare lung responses to experimental Mhp infection in highly susceptible Chenghua pigs and relatively resilient Yorkshire pigs at 28 days post-infection. Using these integrated approaches, we aimed to characterize shared and breed-specific features of immune activation, metabolic state, and tissue organization in the infected lung. Chenghua pigs were characterized by sustained proinflammatory signaling, relative attenuation of interferon-associated defenses, hypoxia- and mTORC1-linked metabolic reprogramming, and extensive remodeling of barrier- and antigen-presentation-related glycoproteins. Together, these findings characterize a coordinated set of immune-metabolic-structural features associated with heightened susceptibility, providing a spatially resolved molecular framework for understanding divergent host responses to Mhp infection.

MATERIALS AND METHODS

Ethical statement

All animal procedures complied with national and institutional guidelines for the care and use of laboratory animals. The study protocol was approved by the Ethics Committee (Approval No. IRB14044) and the Animal Welfare and Use Committee of Sichuan Agricultural University (Permit No. DKY-B20240302).

Animals and experimental design

A total of 24 male Chenghua (CH) and 24 male Yorkshire (YY) nursery pigs were used. At enrollment (50–63 days of age), pigs were clinically healthy and tested negative for African swine fever virus, porcine circovirus type 2, *Mycoplasma hyopneumoniae* (Mhp) and other major pathogens by reverse transcription quantitative polymerase chain reaction (RT-qPCR) and ELISA. Within each breed, pigs were randomly allocated to either the control (CHC, YYC) or infection (CHI, YYI) groups (n=12 per group) and housed individually under identical environmental and management conditions. Detailed individual information, including exact body weight distributions and source farms, is provided in Supplementary Methods and Supplementary Table S1.

Mycoplasma hyopneumoniae challenge and sampling

Experimental infection followed a previously described intratracheal inoculation protocol (Gan et al., 2020). Briefly, pigs in the infected groups received 5 mL of a *M. hyopneumoniae* strain JS (Feng et al., 2010) tissue homogenate (10^8 CCU/mL) by percutaneous intratracheal inoculation, whereas control pigs received 5 mL of sterile PBS via the same route. Pigs were monitored throughout the 28-day experimental period for growth performance and respiratory signs. Nasal swabs and blood samples were collected weekly for quantification of Mhp DNA by RT-qPCR and for measurement of Mhp-specific serum antibodies by enzyme-linked immunosorbent assay (ELISA), respectively (see Supplementary Methods). At 14 and 28 days post-infection (dpi), six pigs per group were humanely euthanized. For spatial transcriptomics and proteomics analyses at 28 dpi, four pigs from each infected group (CHI, *n*=4; YYI, *n*=4) and two pigs from each control group (CHC, *n*=2; YYC, *n*=2) were randomly chosen. These 12 animals constituted the multi-omics cohort. Lesion boundary areas of the left cranial lung lobe from infected animals, or the corresponding anatomical regions from controls, were collected for spatial transcriptomics, and remaining lung tissues from the same animals were snap-frozen for proteomic and N-glycoproteomic analyses.

Lung lesion scoring, histopathological evaluation and serological analysis

Macroscopic lung lesions were scored according to the European Pharmacopoeia system (Pharmacopoeia, 2013). For each lobe, the proportion of visible consolidation was estimated and multiplied by a lobe-specific weighting factor. The total lung lesion score (0–100) was obtained by summing the weighted scores of all lobes. For histopathology, tissue sections were taken from the left cranial lung lobe in all infected animals and from the anatomically corresponding region in controls, as this lobe develops the most consistent lesions in experimental Mhp infection. Lesion and corresponding control areas were fixed in 10% neutral buffered formalin, embedded in paraffin and stained with haematoxylin and eosin (H&E). Pathological features including alveolar structural integrity, inflammatory cell infiltration, edema and hemorrhage were assessed using a semi-quantitative grading system. Each parameter was scored on a 0–4 scale based on lesion severity and extent, and individual scores were summed to obtain a total histopathological score ranging from 0 to 16 (Keenan et al., 2015). Detailed grading criteria are provided in Supplementary Table S2. Serum antibody responses against Mhp were quantified using a commercial indirect ELISA kit. Antibody levels were expressed as sample-to-positive (S/P) values and analysed as continuous variables for all tested animals at each time point. In addition, seropositivity rates were determined based on the manufacturer-recommended cut-off and analyzed separately. Detailed criteria are provided in the Supplementary Methods.

Spatial transcriptomics and downstream analysis

Frozen lung tissue was sectioned at 10 μm and mounted on Visium Spatial Gene Expression Slides (10× Genomics). Sections were fixed, H&E-stained and imaged to capture tissue morphology, followed by on-slide permeabilization, reverse transcription, cDNA amplification and library preparation according to the manufacturer's protocol. Libraries were sequenced on an Illumina NovaSeq 6000 platform (USA). Raw data were processed with Space Ranger v.2.0.0 and aligned to the *Sus scrofa* reference genome (*Sscrofa* 11.1). After quality control, gene expression matrices were normalized using SCTransform (Hafemeister & Satija, 2019), and datasets were integrated in Seurat (v.5.3.0) using the reciprocal PCA workflow (Stuart et al., 2019). Principal component analysis (PCA) and UMAP were used for dimensionality reduction, and unsupervised clustering was performed with the Smart Local Moving (SLM) algorithm. Spatial clusters were annotated to major lung cell populations based on canonical marker genes and spatial context, with key markers listed in Supplementary Table S3.

Differentially expressed genes (DEGs) between conditions or clusters were identified in Seurat using the Wilcoxon rank-sum test with Benjamini–Hochberg correction. Genes with $|\log_2 FC|>1$ and adjusted *P*-value<0.05 were considered significant. Functional enrichment analyses for DEGs used clusterProfiler, and gene set enrichment analysis (GSEA) was conducted with the fgsea package using MSigDB Hallmark gene sets, retaining terms with BH-adjusted *P*-value<0.05. Protein–protein interaction (PPI) networks were constructed from cluster-specific DEGs using the STRING database and visualized in Cytoscape to highlight hub genes. Transcription factor (TF) and pathway activities were inferred with the decoupleR framework integrating DoRothEA and PROGENy resources. Immune cell composition was estimated from spatial transcriptomic data using CIBERSORTx (Newman et al., 2019) with the LM22 leukocyte signature matrix, and spatial gene-immune cell correlations were assessed as described in the Supplementary Methods. Because the LM22 signature matrix is derived from human leukocyte profiles, deconvolution results were interpreted mainly in terms of relative trends rather than absolute cell proportions. Ligand-receptor-mediated cell-cell communication networks were inferred using CellChat (Jin et al., 2021) with CellChatDB.human, and group-wise differences in pathway-level information flow and interaction strength were summarized as $\log_2 FC$. Ligand-receptor interactions were inferred based on human databases, with pig orthologues mapped using Ensembl annotations. Full computational details and parameter settings are provided in Supplementary Methods.

Proteomics and N-glycoproteomics

Label-free quantitative proteomics and N-glycoproteomics were performed on the same 12 animals included in the spatial transcriptomics cohort. Approximately 100 mg of frozen lung tissue per sample was homogenised in urea-based lysis buffer, reduced, alkylated and digested overnight with trypsin. Peptides were desalted and analysed on an EASY-nLC 1200 system coupled to an Orbitrap mass spectrometer using a 120-min gradient in data-dependent acquisition mode. Raw proteomic data were processed with MaxQuant against the *Sus scrofa* reference proteome with a false discovery rate (FDR) of 1% at the peptide and protein levels. Label-free quantification used the MaxLFQ algorithm with "match between runs" enabled. Differentially abundant proteins were defined using $\log_2$-transformed LFQ intensities, with BH-adjusted *P*-value<0.05 and |FC|>1.5.

For N-glycoproteomics, N-glycopeptides were enriched from tryptic digests using zwitterionic hydrophilic interaction chromatography (ZIC-HILIC) and analysed on the same LC-MS/MS platform. N-glycopeptides were identified with MSFragger using a library of 182 N-glycan compositions,

controlling FDR at 1%. Glycans were classified into paucimannose, high-mannose, complex/hybrid, fucosylated and sialylated types. To identify site-specific glycosylation changes independent of protein abundance, we compared site-level and protein-level $\log_2$FC between CHI and YYI pigs and defined "glyco-specific" sites as N-glycosites with significant regulation at the glycopeptide level but not at the corresponding protein level and with a large residual (site-level $\log_2$FC−protein-level $\log_2$FC). Detailed MS settings, data processing parameters and multivariate analyses (including PCA and RandomForest) are provided in Supplementary Methods.

Multiplex immunofluorescence, RT-qPCR and Western blot

Multiplex immunofluorescence was performed on formalin-fixed, paraffin-embedded lung sections using a tyramide signal amplification–based three-color protocol to detect CD68, iNOS and CD206, with DAPI nuclear counterstaining and whole-slide imaging for quantitative analysis. Quantitative real-time PCR (RT-qPCR) was conducted on lung RNA to validate selected genes (*CTSL, SPP1, IL1B, CXCL2, CXCL8, CXCL9, CXCL10, HOPX, BPIFA1, FCN2, LDHA, SOD2, MARCO* and *ISG15*), using *PPIA* and *RPL4* as internal reference genes and the $2^{-\Delta\Delta Ct}$ method for relative quantification. Western blotting was used to assess LDHA protein abundance, with β-actin as a loading control. Detailed experimental procedures, primer sequences and antibody information are provided in Supplementary Methods and Supplementary Table S4.

Statistical analysis

Unless otherwise stated, data are presented as mean±SD. Statistical analyses were performed in R (v.4.4.3). For normally distributed data, Student's *t*-test was used; for non-parametric comparisons, the Wilcoxon rank-sum test was applied. Multiple testing was controlled using the Benjamini–Hochberg method, and adjusted *P*-value<0.05 was considered statistically significant. Specific models for transcription factor and pathway activity inference, immune cell deconvolution and N-glycosite-based RandomForest classification are described in the Supplementary Methods.

RESULTS

Chenghua and Yorkshire pigs show divergent clinical and pathological responses to Mhp infection

Under an identical inoculation dose, Chenghua pigs exhibited more severe clinical and pathological manifestations than Yorkshire pigs. In the Chenghua infected (CHI) pigs, dry cough appeared from 9 dpi and progressed to dyspnea. By 28 dpi, all animals (6/6) displayed marked respiratory distress and extensive lung involvement. In Yorkshire infected (YYI) pigs, clinical signs were delayed until 19 dpi and remained mild. At 28 dpi, four of six infected pigs showed a dry cough without obvious respiratory distress (Supplementary Table S5). Serological and gross pathological changes paralleled these clinical differences. Mhp-specific antibody titers rose in both infected groups but were ~3-fold higher in CHI than in YYI at 14 dpi (P=8.21×10^{-3}; Figure 1A; Supplementary Table S6). The CHI pigs consistently showed higher lung lesion scores from 14 dpi onwards (P<0.01; Figure 1B; Supplementary Table S7). At 28 dpi, CHI pigs exhibited confluent consolidation affecting large lung areas, whereas YYI pigs contained only small, focal lesions (Figure 1C). Despite this, pulmonary Mhp burden measured by RT-qPCR did not differ significantly between breeds (Figure 1D), consistent with an association between disease severity and host response patterns rather than differences in pulmonary pathogen burden.

Histopathology confirmed a much more aggressive disease course in CHI (Figure 1E). At 14 dpi, CHI pigs showed multilobar interstitial pneumonia with disruption of alveolar architecture, dense neutrophilic infiltration and marked airway epithelial damage with ciliary loss. YYI lesions were mild and focal, with limited septal thickening, scattered mononuclear cells and largely preserved airway structure (Figure 1F). By 28 dpi, CHI pigs progressed to chronic diffuse injury with near-complete loss of normal alveolar structure, dense inflammatory and fibroproliferative infiltrates and extensive bronchial epithelial denudation. In contrast, YYI pigs displayed only mild focal lymphocyte and macrophage infiltrates without overt tissue destruction or fibrosis (Figure 1G). Together, these data indicate that under identical exposure, Chenghua pigs develop severe, progressive pneumonia accompanied by marked inflammatory dysregulation, whereas Yorkshire pigs mount a milder, self-limiting response.

Spatial transcriptomics reveals breed-specific spatial heterogeneity in infected lungs

To investigate the molecular basis of these pathological differences, we performed spatial transcriptomics on lung tissue at 28 dpi. After quality control, 16 033 spots with ~3 000 genes per spot were retained (Supplementary Table S8). Unsupervised clustering identified 11 spatial clusters corresponding to distinct structural and immune compartments (Figure 2A). Canonical marker gene expression across clusters guided cluster annotation (Figure 2C). Clusters C1–C4 represented alveolar-capillary units. C1 contained relatively intact alveoli, C2 enriched proliferating/repairing cells, C3 marked type II alveolar epithelial (AT2) cells, and C4 co-expressed haemoglobin, endothelial and epithelial markers, consistent with a transitional AT2-like state. After infection, intact alveolar (C1) and proliferating (C2) regions decreased and AT2-like clusters (C3) expanded in both breeds, with more pronounced shifts in CHI pigs, consistent with the broader extent of alveolar disruption and reactive AT2 expansion (Figure 2B; Supplementary Figure S1A). Structural clusters also included activated fibroblasts (C5), airway-associated club cells, bronchial epithelium and ciliated epithelium along the airway axis (C7–C9), and vascular smooth muscle cells (C10) (Figure 2D). Immune-enriched clusters C0 and C6 were remodeled by infection. C0 comprised monocyte-macrophage-rich regions with acute-phase and lysosomal genes, reflecting activated innate immunity, whereas C6 represented lymphocyte aggregates with high expression of chemokines and T- and B-cell markers and activation of TCR/BCR signaling (Supplementary Figure S1B). Following infection, C0 and C6 expanded more in CHI than in YYI pigs, and spatial maps showed lymphocytes accumulating along the interstitium and around airways (Figure 2B; Supplementary Figure S1A). Overall, Mhp infection induces a shared spatial framework in both breeds, but Chenghua pigs show a greater spatial expansion of inflammatory and lymphoid niches.

Breed-specific inflammatory, metabolic and barrier reprogramming in infected lungs

To establish the infection-associated transcriptional landscape

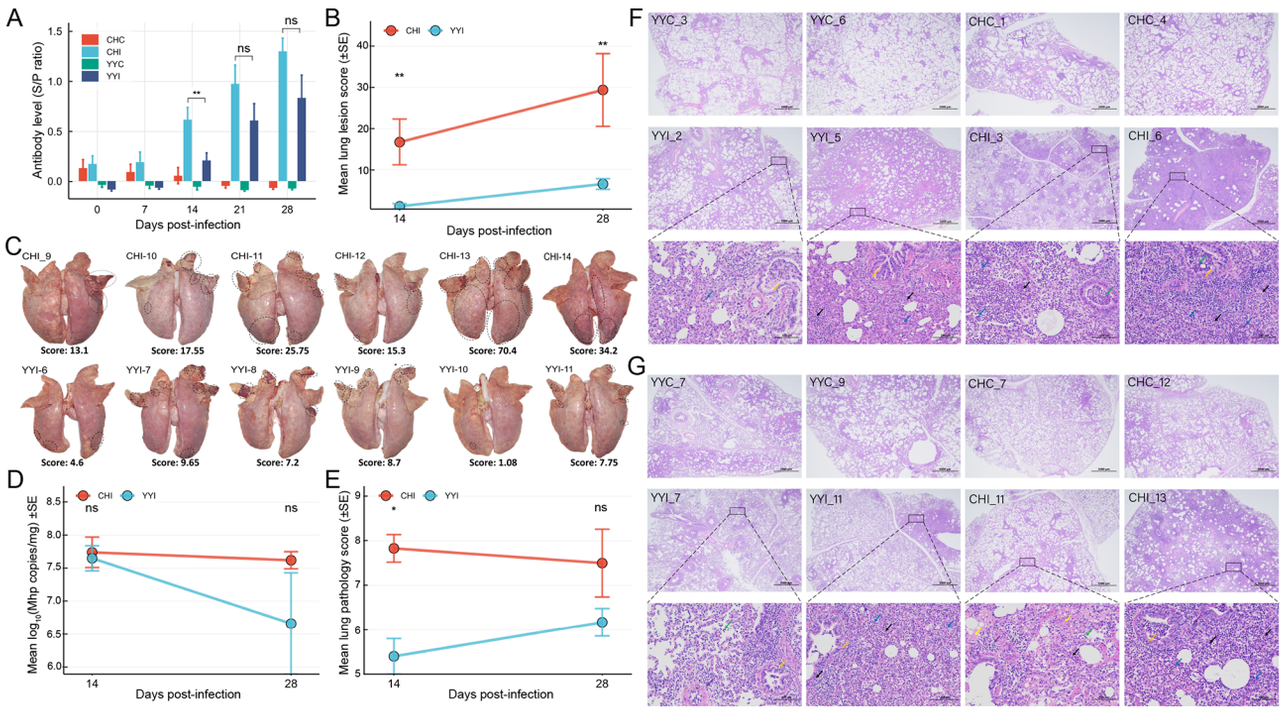


Figure 1 Enhanced disease severity and lung pathology in Chenghua pigs compared with Yorkshire pigs following *Mycoplasma hyopneumoniae* infection

A: Serum Mhp-specific IgG (S/P ratio) from 0 to 28 dpi (n=12 per group at 0, 7, and 14 dpi, except YYI at 14 dpi, n=11; n=6 per group at 21 and 28 dpi). CHI vs. YYI at 14 dpi, P=0.0082. B: Macroscopic lung lesion scores at 14 and 28 dpi (n=6 per group, except YYI at 14 dpi, n=5). CHI vs. YYI, P=0.0080 (14 dpi) and P=0.0022 (28 dpi). C: Representative gross lung photographs; black circles delineate macroscopic lesions. D: Pulmonary Mhp DNA loads (n=4 per group per time point). E: Composite histopathological scores at 14 and 28 dpi (n=6 per group, except YYI at 14 dpi, n=5). CHI vs. YYI at 14 dpi, P=0.0101. F, G: Representative H&E-stained lung sections at 14 dpi (F) and 28 dpi (G); boxed regions (middle row) are magnified in the bottom row. Arrows indicate peribronchiolar and perivascular lymphoid hyperplasia (black), granulocytic infiltration of alveolar septa (blue), airway epithelial necrosis and desquamation (orange), and intraluminal granulocytic exudate (green). Scale bars: 1 000 μm (top and middle rows) and 100 μm (bottom row). All comparisons are CHI vs. YYI at the indicated time point. Mann–Whitney U test, ns: Not significant; *: P<0.05; **: P<0.01. CHC: Chenghua control; CHI: Chenghua infected; YYC: Yorkshire control; YYI: Yorkshire infected.

within each breed, we first compared infected pigs with their respective healthy controls across spatial clusters. In Chenghua pigs, Mhp infection induced broad transcriptional activation across alveolar and immune compartments, characterized by pronounced upregulation of inflammatory mediators and immunometabolic genes, together with a pronounced reduction in genes associated with epithelial, endothelial and barrier maintenance programs (Supplementary Figure S2A). These changes were evident across multiple alveolar clusters and were accompanied by marked induction of acute-phase and stress-response pathways (Supplementary Figure S3A). In contrast, Yorkshire pigs displayed a more restrained transcriptional response to infection. While innate immune and mucosal defense genes were induced, particularly within immune-enriched clusters, structural and vascular integrity–associated gene programs were largely preserved, and interferon-stimulated genes were prominently upregulated in lymphoid niches (Supplementary Figures S2B and S3B). Thus, although both breeds mounted a shared infection response, the balance between inflammation, metabolic adaptation and tissue maintenance differed substantially.

Direct CHI–YYI comparisons across clusters showed that these local differences form part of a coordinated inflammatory–metabolic program in CHI pigs. Proinflammatory and immunometabolic genes, including *IL1B*, the TNF receptor superfamily member-like transcript *LOC102158193* (TNFRSF6-like), *LDHA, ARG1, SPINK1* and *RETN*, consistently ranked among the top upregulated genes across multiple clusters. In contrast, genes involved in epithelial and endothelial structure and barrier maintenance were systemically downregulated in CHI across several clusters, such as *BPIFA1, DMBT1, DISP2* and *MARCO*. Multiple interferon-stimulated genes (ISGs), including *ISG15, CXCL10* and *CXCL11*, showed the most pronounced downregulation in clusters C6 and C8 (Figure 3A). Pathway analysis confirmed significant enrichment of TNFα–NF-κB and IL-6–JAK–STAT3 signaling, together with activation of mTORC1, hypoxia-associated gene sets, unfolded protein response and epithelial–mesenchymal transition programs in Chenghua pigs, while IFN-I responses were globally attenuated (Figure 3B). To place these expression changes into a regulatory context, we next examined protein-protein interaction networks and transcription factor activity associated with the differentially expressed genes. Protein–protein interaction networks identified *IL1B, CXCL2, CXCL10* and *ISG15* as central nodes in the differential gene networks for C3 and C6, respectively (Figure 3C). Inflammatory and stress-related transcription factors (such as *HIF1A*, RELA, ATF4/*ATF6, CEBPB, STAT3* and *NFKB1*) showed increased activity in CHI, whereas antiviral and epithelial homeostatic regulators including *IRF9, STAT2* and *FOXA2* were suppressed (Figure 3D, F). In YYI, these factors changed to a lesser extent, and key interferon-related

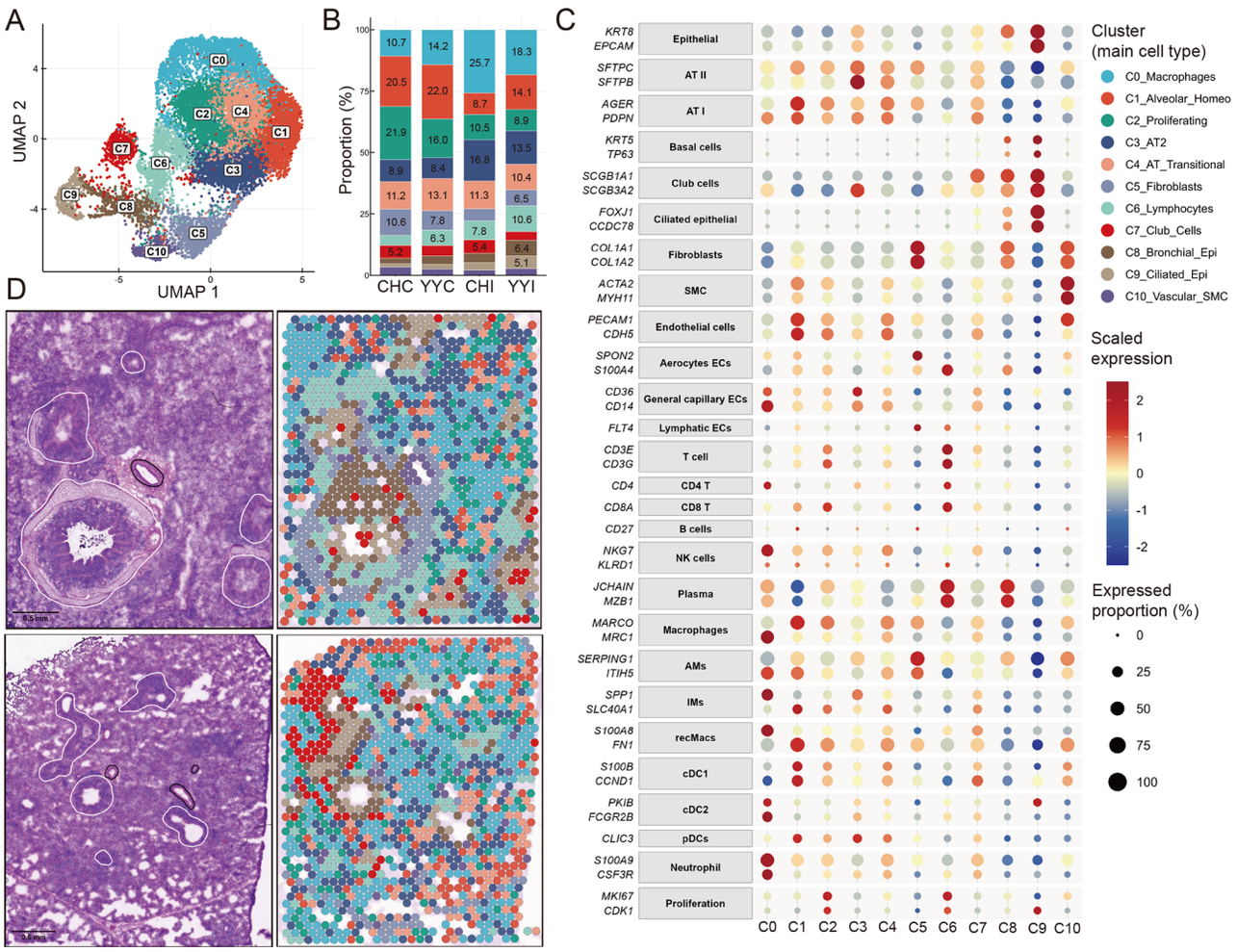


Figure 2 Spatial transcriptomics defines lung structural and immune niches and reveals infection-induced remodeling across breeds

A: UMAP projection of combined spatial transcriptomic data, identifying 11 spatial clusters (C0–C10), each represented by a distinct color. Each cluster is annotated with its predominant cell type. B: Cluster composition across experimental groups. Stacked bar plots showing the proportion of each spatial cluster in CHC, CHI, YYC, and YYI pigs. C: Dot plot of canonical cell type marker gene expression across spatial clusters. Rows represent marker genes grouped by cell lineage, and columns represent spatial clusters (C0–C10). Dot color indicates scaled average expression (blue–red, low to high), and dot size reflects the proportion of spots expressing each gene within the respective cluster. D: Spatial mapping of cluster organization in representative infected lungs from Yorkshire (YYI_11, upper) and Chenghua (CHI_10, lower) pigs. Left panels show the corresponding H&E-stained sections (scale bar: 0.5 mm), with white circles indicating bronchi and bronchioles and black circles highlighting capillary-rich alveolar regions. Right panels display spatial transcriptomic maps of the same sections, with spots colored by cluster identity (C0–C10). CHC: Chenghua control; CHI: Chenghua infected; YYC: Yorkshire control; YYI: Yorkshire infected.

regulators tended to be maintained or modestly increased (Figure 3E). These breed-specific programs and the attenuated interferon response in CHI were independently confirmed by RT-qPCR of key inflammatory, structural, mucosal defense and interferon-stimulated genes (Supplementary Figure S4A). Overall, Chenghua pigs with high disease susceptibility exhibited a lung-wide program characterized by amplified NF-κB/STAT3- and hypoxia-associated inflammation pathways, metabolic reprogramming and attenuation of interferon and barrier-related gene networks.

Defective interferon responses and reshaping of the immune cell landscape in Chenghua pigs

To dissect cellular contributors to these divergent responses, we used CIBERSORTx to infer the relative abundances of 22 immune cell subsets in infected lungs (Supplementary Figure S5A). CHI pigs showed marked expansion of M0 nonpolarized and M2 macrophages, plasma cells and activated mast cells, with proportions significantly higher than in YYI pigs, whereas M1 macrophages, monocytes, $CD8^+$ T cells and regulatory T cells were relatively reduced and significantly lower than in YYI pigs (Figure 4A). Multiplex immunofluorescence for CD68, iNOS and CD206 validated this macrophage polarization pattern. In CHI pigs, most $CD68^+$ macrophages co-expressed the M2 marker CD206, and were broadly distributed across alveolar regions. $iNOS^+$ cells represented only a minor fraction, and were predominantly localized along the airway epithelium (Figure 4B). Although the proportions of both $CD206^+$ and $iNOS^+$ cells among $CD68^+$ macrophages were higher in CHI than in YYI pigs (Figure 4C), per-cell iNOS intensity was markedly lower in CHI pigs (Figure 4D). Together, these data indicate an M2-dominated, low-iNOS macrophage compartment in CHI pigs, consistent with reduced cytotoxic effector capacity and a shift towards heightened inflammatory and humoral activation.

Spatial correlation analysis linked these cellular changes to local cytokine and interferon signatures. *IL1B* expression

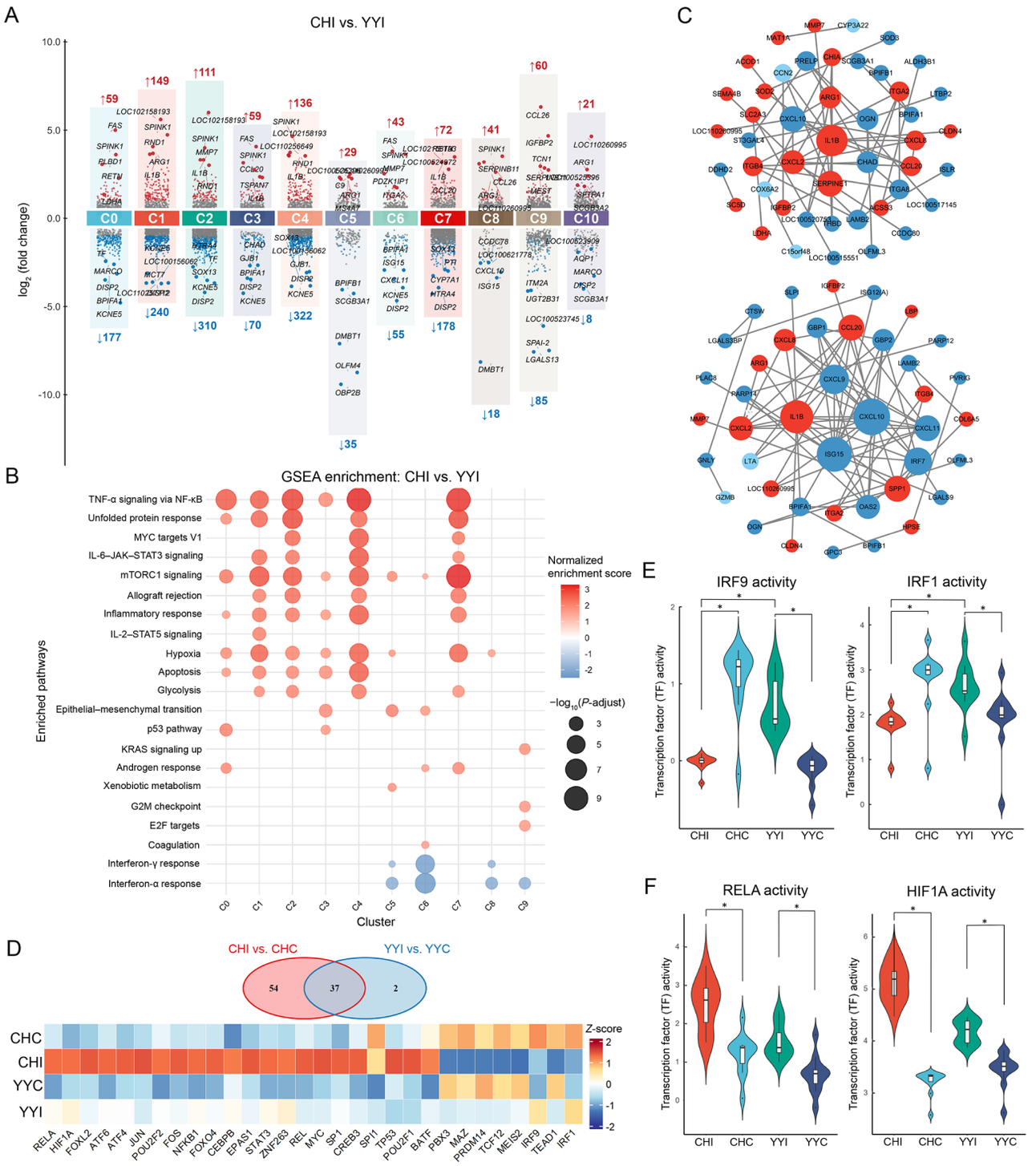


Figure 3 Coordinated inflammatory, metabolic, and regulatory reprogramming distinguishes Chenghua from Yorkshire pigs following infection

A: Volcano plots showing differential gene expression between CHI and YYI across spatial clusters (C0–C10). Red and blue dots represent significantly upregulated and downregulated genes. Numbers indicate the number of significantly DEGs per cluster, and representative high-effect genes are labelled. B: Gene set enrichment analysis (GSEA) of HALLMARK pathways across spatial clusters comparing CHI with YYI. Dot size represents $-\log_{10}$(adjusted *P*-value), and color indicates normalized enrichment score (NES), with red denoting positive enrichment and blue negative enrichment in CHI vs. YYI. C: Protein-protein interaction (PPI) networks constructed from DEGs in clusters C3 (top) and C6 (bottom). Node color indicates expression change (red: Upregulated; blue: Downregulated in CHI vs. YYI), and node size reflects connectivity degree within the network. D: Transcription factor (TF) activity analysis. Top: Venn diagram showing overlap of significantly altered TFs between CHI vs. CHC and YYI vs. YYC comparisons. Bottom: Heatmap of the top 30 TFs ranked by absolute activity difference in the breed–infection analysis. Colors represent *Z*-score–normalized TF activities averaged across spatial clusters. E, F: Violin plots showing distributions of inferred TF activities across experimental groups for antiviral regulators (E) and inflammatory-associated regulators (F). *: $P<0.05$. CHC: Chenghua control; CHI: Chenghua infected; YYC: Yorkshire control; YYI: Yorkshire infected.

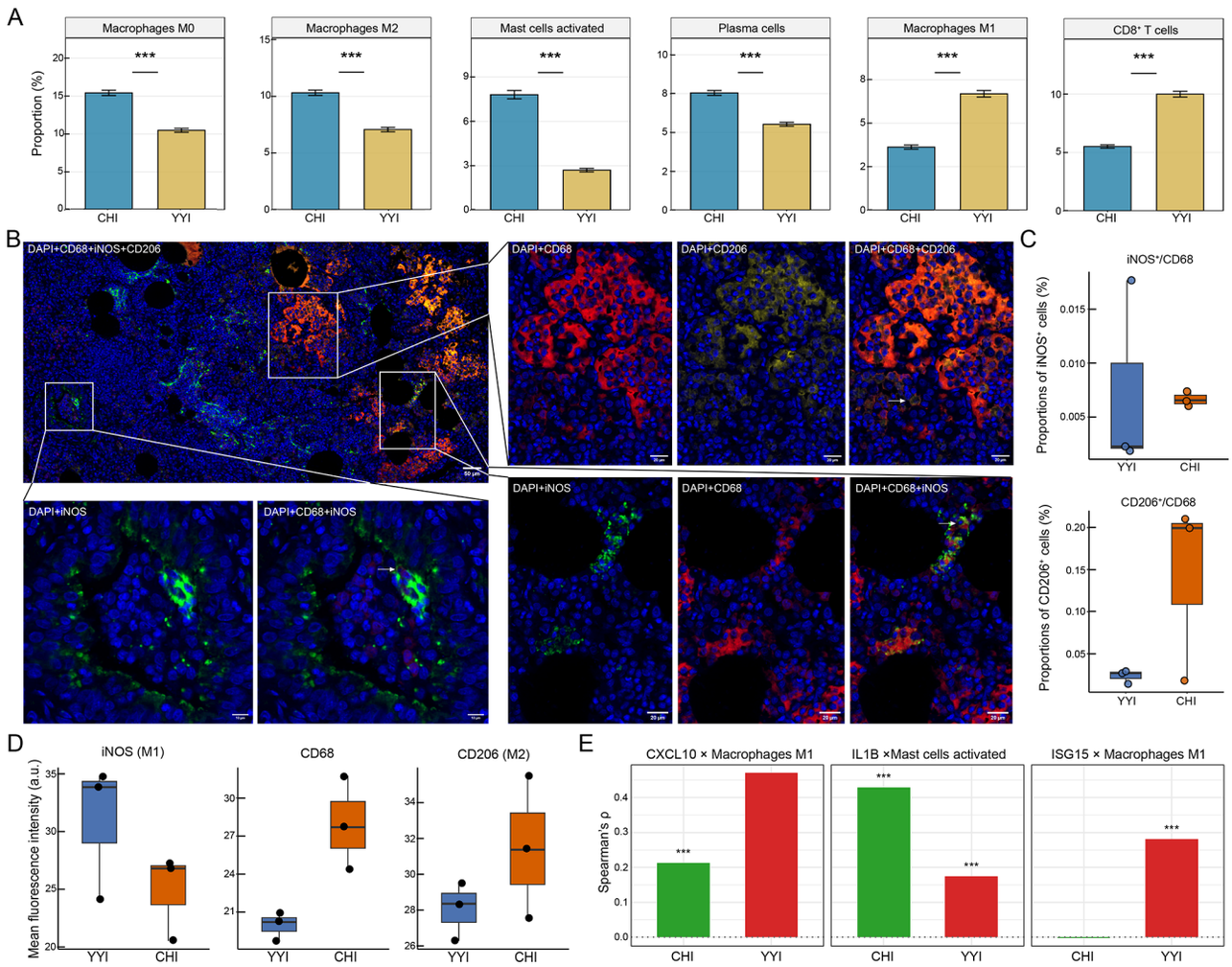


Figure 4 Impaired interferon-associated immune organization and macrophage polarization in Chenghua pig lungs

A: Bar plots showing the relative proportions of immune cell subsets in CHI and YYI pigs. B: Representative multiplex immunofluorescence images of CHI pig lung sections. Upper-left panels: Low-magnification merged overview; lower-left panels: High-magnification view of a bronchiole-associated region; upper-right panels: High-magnification view of an alveolar region; lower-right panels: High-magnification view of an alveolar region. Arrowheads indicate representative co-localization, and scale bars are indicated in each panel. C: Proportions of iNOS$^+$ (M1-like) and CD206$^+$ (M2-like) cells among CD68$^+$ macrophages in YYI and CHI pigs. Each dot represents one animal (n=3). D: Mean fluorescence intensity of iNOS, CD68, and CD206 in YYI and CHI pigs (n=3). E: Bar plots showing breed-stratified Spearman correlation coefficients between *IL1B* and activated mast cell abundance, and between *CXCL10* or *ISG15* and M1 macrophage abundance. ***: P<0.001. CHC: Chenghua control; CHI: Chenghua infected; YYC: Yorkshire control; YYI: Yorkshire infected.

showed a positive correlation with activated mast cell abundance, and *IL1B*-high regions were preferentially enriched for mast cells (Supplementary Figure S5B). This enrichment was particularly pronounced in CHI pigs (Figure 4E), suggesting that mast cells contribute to the maintenance of a highly proinflammatory microenvironment in susceptible pigs. In contrast, the interferon-centered *ISG15-CXCL10* module exhibited marked breed-specific associations. In YYI pigs, expression of *ISG15* and *CXCL10* correlated with M1 macrophage abundance, and M1 macrophages were enriched within *ISG15/CXCL10*-high regions (Supplementary Figure S5C). These spatial relationships are consistent with coordinated coupling between interferon signaling and M1 polarization, and with *CXCL10*-mediated recruitment of effector immune cells. In CHI pigs, however, the correlation between *ISG15* expression and M1 macrophages was markedly reduced. In addition, the association between *CXCL10* and M1 macrophages was substantially weakened, consistent with the reduced expression of both *ISG15* and *CXCL10* (Figure 4E). This spatial decoupling is consistent with an attenuation of the spatial coupling between interferon signaling and M1 polarization, and with limited CXCR3$^+$ CD8$^+$ T cells recruitment (Supplementary Figure S5D), collectively reflecting the M0/M2-skewed, interferon-deficient immune landscape observed in Chenghua pigs.

Rewiring of the pulmonary cell-cell communication network after infection

We next inferred ligand–receptor-mediated cell–cell communication using spatial transcriptomic data. Globally, total communication strength in CHI pigs decreased by approximately 50% relative to CHC based on aggregated communication probabilities estimated by CellChat, whereas YYI pigs showed only a minor reduction compared with healthy pigs and even gained additional active pathways (Figure 5A). Most interactions in CHI were weakened relative to YYI, with only a few clusters, such as alveolar units,

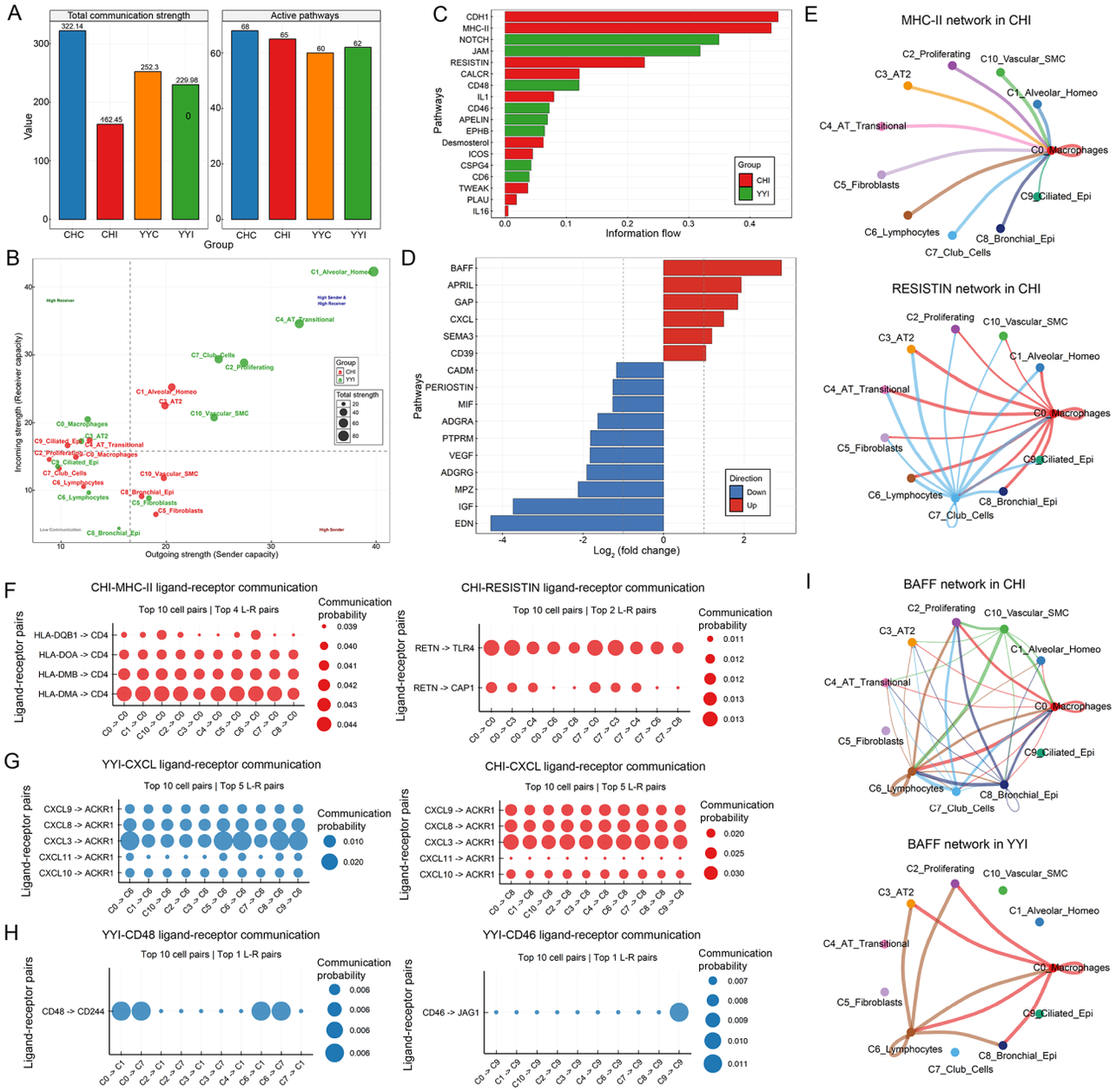


Figure 5 Global disruption and breed-specific rewiring of ligand–receptor-mediated cell–cell communication networks

A: Core communication metrics across CHC, CHI, YYC, and YYI. B: Quadrant analysis of per-cluster sender (outgoing) vs. receiver (incoming) communication capacity in CHI and YYI; dashed lines indicate median values on each axis. C: Group-specific signaling pathways ranked by information flow in CHI vs. YYI. D: Log_2 (fold change) in information flow for pathways common to CHI and YYI (positive values favor CHI; negative values favor YYI). E: Aggregated MHC-II and RESISTIN signaling networks in CHI; nodes denote cell clusters, and edge thickness reflects pathway-specific communication probability. F: Bubble plots for MHC-II and RESISTIN signaling in CHI. G: Bubble plots for CXCL chemokine signaling in CHI and YYI. H: Bubble plots for CD48 and CD46 signaling in YYI. For bubble plots (F–H), the x-axis shows cell–cell pairs, the y-axis shows ligand–receptor pairs, and bubble size represents inferred communication probability. I: BAFF signaling networks in CHI and YYI. CHC: Chenghua control; CHI: Chenghua infected; YYC: Yorkshire control; YYI: Yorkshire infected.

retaining comparatively higher communication activity (Figure 5B). These observations suggest a global disruption of pulmonary communication networks in CHI pigs but preserved or diversified signaling in YYI pigs. Despite these differences, both breeds shared a core set of infection-induced pathways. Proinflammatory axes centered on SPP1 and CypA, myeloid-related CSF3 signaling, B-cell factors BAFF/APRIL and the ectonucleotidase CD39 were upregulated in both YYI and CHI, whereas pathways related to extracellular matrix, basement membrane, endothelial integrity and tissue homeostasis were synchronously downregulated (Supplementary Figures S6A, B). Superimposed on this core, breed-specific rewiring was evident. Relative to healthy Chenghua controls, CHI pigs gained multiple newly activated pathways, with epithelial adhesion (CDH1-centered) and MHC-II antigen presentation showing high information flow, whereas YYI gained fewer new pathways, including PROS1, VISFATIN/NAMPT and more moderate BAFF/APRIL signaling (Supplementary Figures S6C, D). Direct CHI–YYI comparison identified MHC-II and RESISTIN signaling and CXCL and IL-1 axes as more active in CHI, consistent with heightened inflammatory signaling in susceptible pigs (Figure 5C, D).

Mapping these axes to cell types revealed that in CHI pigs, MHC-II-associated molecules were broadly expressed by epithelial, endothelial and stromal cells and converged on macrophage- and lymphocyte-rich clusters. RESISTIN (RETN) was mainly produced by C0 macrophages and C7 club cells and signalled widely via CAP1, supporting a proinflammatory, hyper-metabolic milieu (Figure 5E, F). CXCL chemokine signaling also differed between breeds. In CHI, CXCL ligands from macrophages and lymphocytes targeted bronchial epithelium, forming macrophage/lymphocyte-to-epithelium chemotactic loops. In YYI, CXCL signaling arose predominantly from lymphocytes and structural cells and was directed mainly towards lymphocytes themselves, consistent with more confined lymphoid aggregates and limited epithelial damage (Figure 5G). In addition to preferential expansion of proinflammatory pathways, CHI selectively lost a broad set of homeostatic signals, including ECM and basement membrane pathways (Supplementary Figure S5C). NOTCH and JAM pathways were activated in YYI and were primarily driven by alveolar epithelial clusters. In contrast, these epithelial-centered communication hubs were markedly reduced or partially absent in CHI (Supplementary Figure S6E).

CD46 and CD48 are regulators of complement activity and immune effector functions. Cell–cell communication analysis showed that both CD46 and CD48 signaling exhibited relatively high communication activity in YYI pigs compared with CHI, consistent with preserved epithelial–immune regulatory interactions under inflammatory conditions. CD48 signaling was predominantly initiated by multiple subsets of alveolar epithelial cells and directed toward proliferative epithelial cells (C2) and secretory epithelial cells (C7), whereas CD46 signaling was mainly mediated by ciliated airway epithelial cells and converged on the C9 cluster (Figure 5H). Among pathways upregulated in both breeds, the BAFF/APRIL axis displayed substantially higher information flow in CHI, with ligand sources extending beyond immune cells to include vascular smooth muscle cells and airway epithelial cells, and with signals preferentially directed toward lymphocytes and macrophages. This communication pattern was consistent with the prominent plasma-cell expansion observed in CHI, suggesting that BAFF/APRIL-B-cell signaling may represent a characteristic immunological feature of the susceptible phenotype (Figure 5I; Supplementary Figure S6F).

Proteomic and N-glycoproteomic remodeling underlies breed-specific barrier failure and immune disequilibrium

To validate and extend the spatial transcriptomic findings at the protein level, we performed integrated proteomic profiling. Differential proteomic analysis demonstrated that CHI pigs experienced more extensive and systematic alterations at the protein level (Supplementary Figure S7A). In CHI vs. CHC, the lung proteome revealed pronounced disruption of the alveolar–capillary barrier, characterized by coordinated downregulation of endothelial junction, tight junction, and basement membrane/extracellular matrix components, including FN1, CLDN18, PECAM1 and CDH5 (Figure 6A). Pathways associated with epithelial-mesenchymal transition (EMT) were globally downregulated in CHI compared to YYI (Figure 6B). Beyond barrier failure, CHI pigs exhibited coordinated activation of innate inflammatory modules, with increased abundance of neutrophil degranulation proteins such as MPO, ELANE, PRTN3, AZU1 and S100A8/A9, as well as increased abundance of plasma cell–associated immunoglobulin components and ER stress–related chaperones including MZB1 and HSPA5 (Figure 6A). Glycolytic and anabolic enzymes were coordinately upregulated in CHI relative to CHC and tended to be higher than in YYI for key nodes such as LDHA and PKM, indicating hypoxia-associated metabolic reprogramming and engagement of nutrient-sensing pathways rather than simple suppression of oxidative phosphorylation (Figure 6A, B). Targeted Western blot analysis confirmed robust LDHA elevation in CHI pigs (P=7.39×10^{-4}), whereas YYI and YYC samples showed only modest increases (Supplementary Figures S4B, C). In parallel, antiviral interferon signaling appeared only partially activated. Several type I IFN-inducible proteins were reduced in CHI vs. CHC (STAT2, UBE2L6, and IFI44L), whereas YYI vs. YYC showed increased interferon- and antigen-processing components, pointing to a perturbed cGAS–STING–STAT2 axis and fragmented ISG induction in CHI (Figure 6C; Supplementary Figure S7B). To quantitatively assess transcript–protein concordance, we performed systematic concordance analyses for CHI vs. CHC, YYI vs. YYC and CHI vs. YYI comparisons (Supplementary Tables S9–S11). In CHI vs. CHC, a substantial proportion of spatially differentially expressed genes defining barrier integrity, neutrophil activation, mucosal defense and metabolic modules exhibited concordant directional changes at the protein level. In contrast, concordance was markedly reduced in YYI vs. YYC and CHI vs. YYI comparisons. In addition, although RT-qPCR validated differential expression of multiple key genes identified by spatial transcriptomics, several of these genes did not show concordant changes at the protein level, underscoring that cell- and region-specific transcriptional alterations revealed by spatial profiling are only partially reflected in bulk tissue proteomic measurements. Overall, the proteomic data mirror the spatial transcriptomic patterns and highlight a characteristic combination of extensive barrier disruption, neutrophil- and B-cell-associated inflammatory responses, metabolic rewiring and incomplete interferon responses in CHI pigs.

To complement global proteomic changes, we performed site-specific N-glycoproteomic profiling of infected and control pigs. In total, >7 000 intact glycopeptides mapping to >1 400 N-glycosylation sites on 768 proteins were identified (Supplementary Figure S7E). The overlap of regulated N-glycosylation sites between Chenghua and Yorkshire pigs was limited, indicating distinct and breed-specific N-glycan responses (Supplementary Figure S7D). To identify glycosylation changes independent of protein abundance, we integrated N-glycosite and protein-level fold changes using a residual measure. This approach enabled the identification of “glyco-specific” sites, where N-glycan regulation was pronounced despite relatively stable parent protein levels.

In CHI pigs, glyco-specific sites were enriched on barrier and adhesion proteins highlighted by spatial transcriptomics and global proteomics. These included ECM and basement-membrane scaffolds (e.g., FN1, laminins, HSPG2), small leucine-rich proteoglycans, integrin subunits and GPI-anchored receptors, as well as on neutrophil, phagocytic and humoral effectors (Supplementary Figure S7F). At these loci, N-glycosylation frequently changed by more than one $\log_2$ unit beyond the corresponding protein. This pattern points to glycan-level alterations that are disproportionately pronounced, relative to protein abundance, in components of the integrin–ECM basement-membrane axis as well as

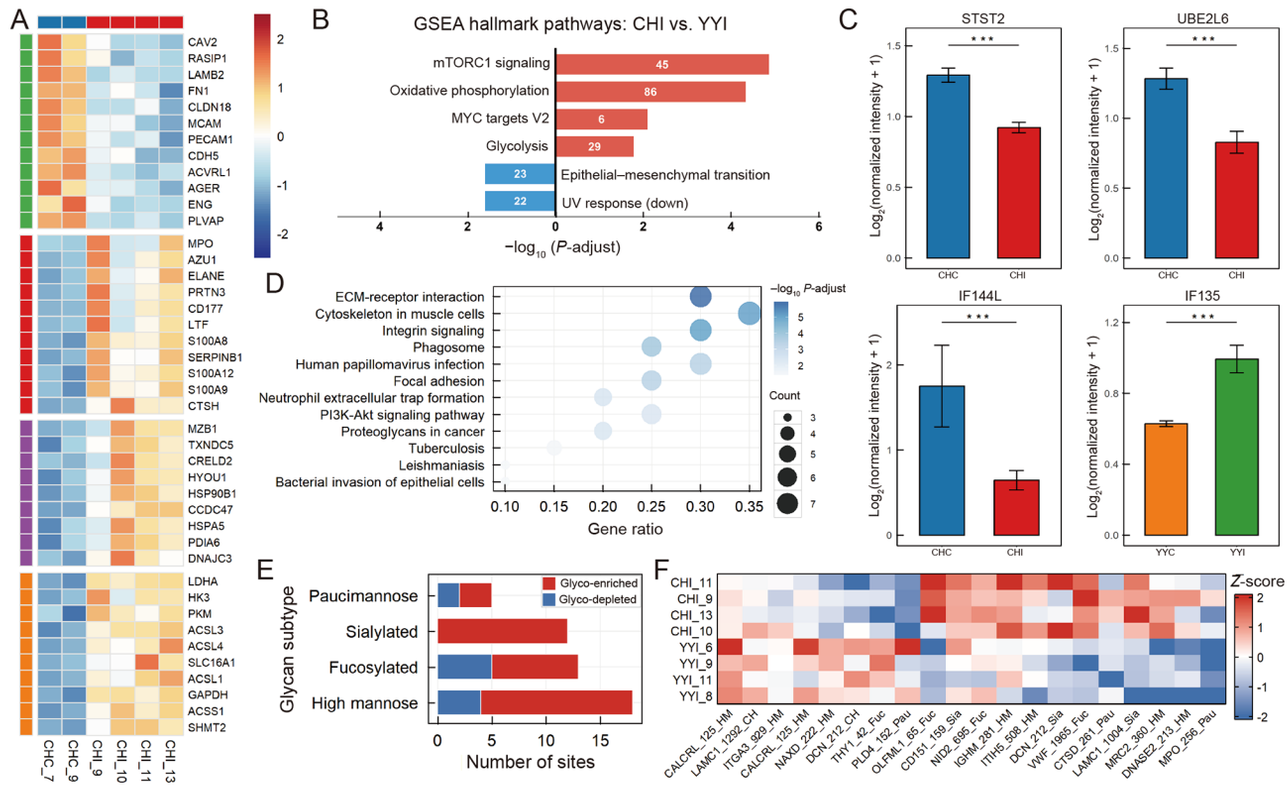


Figure 6 Proteomic and N-glycoproteomic remodeling reveals breed-specific barrier disruption and immune dysregulation in Mhp-infected pigs

A: Heatmap of predefined protein modules related to the alveolar–capillary barrier, neutrophil degranulation, plasma cell/ER stress, and metabolic remodeling in the CHI vs. CHC comparison. Rows represent proteins, and columns represent individual samples. B: MSigDB Hallmark gene set enrichment analysis of differentially expressed proteins in the CHI vs. YYI comparison. Positive normalized enrichment scores (NES, red) indicate pathways activated in CHI, whereas negative NES (blue) indicate pathways activated in YYI. C: Bar plots showing normalized protein abundance of representative interferon/antiviral and antigen-processing components across groups (mean±SEM). Statistical significance was assessed using two-sided unpaired *t*-tests (***: $P<0.001$), shown as a bubble plot. E: Distribution of glycan types among glyco-specific sites. Bar plots summarize the number of glyco-enriched (red) and glyco-depleted (blue) sites for each glycan category. F: Random forest-derived N-glycosylation features distinguishing CHI and YYI pigs. The heatmap shows the top 20 N-glycosylation features ranked by importance.

granulocyte- and B-cell-associated proteins. Genes carrying residual-positive or residual-negative sites were enriched for pathways centered on ECM–receptor interaction, focal adhesion, cytoskeleton organization, phagosome and neutrophil extracellular trap formation, together with PI3K–Akt signaling (Figure 6D). Stratification by glycan subtype revealed a non-random reshaping of the N-glycan repertoire. Sialylated sites showed a predominant upward bias, with selective enhancement relative to protein abundance. High-mannose and fucosylated sites also tended to increase, whereas paucimannose sites were near neutral and complex/hybrid glycans tended to exhibit negative residuals (Figure 6E). Thus, CHI pigs exhibit a sialylation-biased and, to a lesser extent, high-mannose/fucosylation-biased N-glycan reprogramming with relative loss of complex/hybrid structures.

In contrast, YYI pigs displayed N-glycan changes more compatible with controlled repair, including increased high-mannose glycosylation at M6PR, enhanced glycosylation of IGF2R, PSAP and other lysosomal glycoproteins, and increased glycosylation of several collagens and small leucine-rich proteoglycans, accompanied by increased N-glycosylation of ECM components and relatively limited changes in neutrophil effector glycosylation (Supplementary Figure S7D). A RandomForest classifier highlighted N-glycosites on ECM/adhesion and neutrophil/B-cell effector proteins among the most informative features distinguishing the two breeds (Figure 6F). Direct comparison also revealed reduced N-glycosylation at key ENPP1 and MHC-II sites in CHI, paralleling decreased protein levels and pointing to additional impairment of purinergic and antigen-presentation checkpoints at the glycan layer (Supplementary Figure S7C). Integrating proteomic and N-glycoproteomic data revealed that high disease susceptibility in Chenghua pigs is associated with sustained neutrophil degranulation, exaggerated B-cell and plasma-cell responses, and ER-stress-linked metabolic reprogramming. This phenotype was further characterized by multilayer loss and glycan-centered remodeling of alveolar-capillary barrier proteins, together with incomplete engagement of interferon, antigen-presentation and ENPP1-mediated purinergic pathways. In contrast, Yorkshire pigs exhibit more limited proteomic perturbations, a relatively intact IFN–immunoproteasome and MHC-II axis, and ECM/N-glycan remodeling characterized by more limited structural disruption and distinct glycosylation patterns compared with Chenghua pigs.

DISCUSSION

Under a standardized Mhp challenge, Chenghua and Yorkshire pigs harbored comparable pulmonary bacterial loads, yet differed markedly in clinical manifestations, lesion

severity and tissue damage. This dissociation between pathogen burden and pathological outcome indicates that disease severity is not determined by bacterial expansion alone, but by how host immune and tissue responses are organized within the infected lung (Figure 1). Breed-dependent differences in susceptibility have been described across multiple porcine disease models, including respiratory viral infections and inflammatory conditions, supporting the view that host background plays a central role in regulating pulmonary inflammation and its resolution (Liang et al., 2016; Zhao et al., 2022). Although Chenghua pigs exhibited lower body weight at enrollment, this reflects the characteristically slower growth rate of this Chinese indigenous breed relative to Yorkshire rather than a developmental abnormality. Pulmonary immune maturation in pigs follows an age-dependent program, with alveolarization largely completed within the first two postnatal weeks regardless of body weight (Dickie et al., 2009). Accordingly, all animals were age-matched at 50–63 days, exposed to identical infectious conditions and maintained comparable pulmonary Mhp loads, arguing against differences in exposure or pathogen replication as primary explanations. Instead, divergent outcomes likely reflect intrinsic differences in immune coordination and tissue resilience shaped by long-term breed-specific selection. Consistent with this view, Chinese indigenous pigs and Western commercial breeds have experienced distinct domestication trajectories, with selection in Western lines prioritising growth traits and Chinese local breeds retaining greater diversity at immune-related loci involved in inflammatory regulation and mucosal defense (Zhang et al., 2018).

In the lung, immune activation and tissue injury emerge from the interplay between host genetic background, pathogen behavior and the local microbial environment. Increasing evidence from porcine respiratory studies indicates that differences in lung microbial composition and functional potential can modulate inflammatory tone and influence disease severity during infection (Li et al., 2024; Meyns et al., 2007; Woolley et al., 2012). Beyond overall microbial composition, local bacterial activity, spatial distribution of infection and temporal dynamics have also been shown to shape host responses in the infected lung (Lim et al., 2025). Although the present study does not directly characterize microbial communities, our spatial analysis at a defined late stage of infection captures the integrated outcome of these interacting factors. By focusing on a well-established late stage of infection, our spatial analyses capture how early host–pathogen interactions consolidate into stable, breed-specific immune architectures. In resistant Yorkshire pigs, inflammatory activity remains spatially confined, alveolar–capillary units preserve barrier-related gene expression and interferon-associated programs remain active within immune hubs. In contrast, susceptible Chenghua pigs exhibit lung-wide activation of NF-κB- and STAT3-linked inflammatory and metabolic pathways across immune and structural compartments, accompanied by broad suppression of epithelial adhesion, interferon signaling and barrier maintenance. Such spatial expansion of inflammation beyond focal niches has been linked to progressive tissue injury in diverse chronic lung diseases, where failure to compartmentalize inflammatory responses predisposes to diffuse structural collapse (De Zuani et al., 2024; Mayr et al., 2024). Our data therefore suggest that susceptibility to Mhp infection is associated not with the presence of inflammation per se, but with loss of its spatial containment.

Across spatial clusters, the most consistent molecular distinction between breeds involves an interferon-related module centered on *ISG15* and *CXCL10*. In Yorkshire pigs, canonical interferon-stimulated genes and their upstream regulators remain active, and spatial alignment between interferon signaling, M1-like macrophage signatures and CD8-associated transcripts is preserved. The CXCL9/10/11–CXCR3 axis is widely recognized as a key link between type I/II interferon signaling (Tong et al., 2022), M1 macrophage polarization (Li et al., 2022) and recruitment of $CXCR3^+$ $CD8^+$ T cells (Tang et al., 2022), and is associated with effective cytotoxic responses and favorable outcomes in infection and cancer (Wang et al., 2022). In Chenghua pigs, attenuation of *ISG15* and *CXCL10* expression and loss of their spatial coupling with cytotoxic immune signatures indicate disruption of this interferon–chemokine axis. Similar uncoupling of interferon signaling from cytotoxic effector recruitment has been described in severe viral pneumonias, including COVID-19, where bystander inflammation coexists with impaired antiviral immunity (Rendeiro et al., 2021). These parallels suggest that failure to maintain interferon-centered immune coordination may represent a shared feature underlying severe lung pathology, in line with prior breed-comparison studies of Mhp infection (Ni et al., 2019; Sakuma et al., 2020; Sato et al., 2016).

Immune profiling further reveals a profoundly imbalanced cellular landscape in Chenghua pigs (Figure 4), characterized by expansion of M0 and M2 macrophages, plasma cells and activated mast cells, together with reduced representation of M1 macrophages, monocytes, $CD8^+$ T cells and regulatory T cells. Rather than reflecting a simple failure of immunity, this pattern suggests a shift from cytotoxic control towards humoral- and inflammation-dominated amplification. Such skewing of myeloid and lymphoid compartments is expected to constrain cytotoxic and bactericidal functions while favoring chronic inflammatory signaling. Similar immune configurations have been described in persistent inflammatory lung diseases, where ineffective clearance coexists with sustained tissue injury. Spatially, *IL1B* expression closely co-localizes with activated mast cells, suggesting that mast cells may contribute to the maintenance of inflammatory niches through IL-1 family cytokines, consistent with reports of mast cell–IL-1 circuits in chronic airway disease (Holtzman et al., 2014). Within this imbalanced immune environment, enhanced BAFF/APRIL signaling emerges as a prominent feature of the susceptible phenotype (Figure 5I). In Chenghua pigs, TNFSF13B (BAFF) and TNFSF13 (APRIL) signals are produced not only by macrophages and lymphocytes but also by structural cells such as airway epithelium and smooth muscle, and their receptors are broadly expressed in B-cell- and plasma cell-rich regions. BAFF-driven B-cell persistence and plasma-cell accumulation have been implicated in ectopic lymphoid organization and fibrotic remodeling in chronic lung disease, including common variable immunodeficiency-associated interstitial lung disease (Maglione et al., 2019). Consistent with this literature, our proteomic data indicate ER stress and upregulation of plasma-cell chaperones in susceptible pigs. These observations are consistent with a model in which elevated BAFF/APRIL signaling contributes to humoral-centric immune amplification, potentially sustaining inflammation and tissue remodeling under conditions of weakened cytotoxic

control (Lim et al., 2020).

Neutrophil responses further distinguish resistant and susceptible outcomes. In Chenghua pigs, neutrophils exhibit a degranulation-dominant program marked by elevated expression of classical granule proteins, iron-binding molecules and S100 alarmins, with comparatively limited induction of protective inhibitors (Figure 6A). Similar neutrophil states have been linked to severe tissue damage and neutrophil extracellular trap (NET) formation in acute lung injury and acute respiratory distress syndrome (Keir & Chalmers, 2022; Twaddell et al., 2019), where NET-associated proteases and nucleic acids amplify thromboinflammation and epithelial and endothelial injury (Sha et al., 2024). Experimental studies further suggest that excessive NET formation can impair autophagic flux and epitranscriptomic regulation and thereby aggravate sepsis-related lung injury (Qu et al., 2022). Although neutrophils are increasingly recognized as a heterogeneous population, with subsets capable of promoting resolution and tissue repair under appropriate regulatory conditions (Rizo-Téllez & Filep, 2024), the predominance of a degranulation-heavy neutrophil state in Chenghua pigs therefore likely contributes to sustained tissue injury rather than effective resolution.

Our proteomic and N-glycoproteomic data indicate multi-layer destabilization of the ECM receptor axis, cell–cell junctions and basement membrane in Chenghua pigs. Coordinated reductions and glycan-centered remodeling of laminins, fibronectin and type IV and VI collagens suggest compromised barrier integrity (Figure 6). The observed shift towards sialylated and high-mannose N-glycan structures, together with relative loss of complex and hybrid glycans, parallels patterns reported in fibrotic lung disease where altered glycosylation has been linked to changes in ECM mechanics, growth factor availability and immune cell adhesion (Drzewicka & Zasłona, 2024; Nizamoglu & Burgess, 2021). These findings suggest that structural vulnerability in susceptible pigs may be reflected not only at the protein level but also through altered post-translational modification landscapes. Beyond structural components, several immune-associated molecules exhibit pronounced breed-dependent changes in abundance and N-glycosylation. Altered glycosylation of FCGR3A, an Fc receptor mediating antibody-dependent cellular cytotoxicity, is known to modulate effector-cell activation (Kremer et al., 2024). Upregulation of FUT8 in Chenghua pigs may further influence core fucosylation of immune glycoproteins, adding an additional regulatory layer to interferon-associated responses (Huang et al., 2021; Liu et al., 2024). In parallel, ENPP1 and certain MHC-II molecules show concordant reductions in protein abundance and N-glycosylation in Chenghua pigs. ENPP1 functions as a key regulator of extracellular cGAMP and ATP metabolism and has been proposed as an innate immune checkpoint in other contexts (Wang et al., 2023). Reduced ENPP1 and MHC-II integrity may therefore be associated with impaired antigen presentation and dysregulated innate signaling, consistent with the fragmented interferon–antigen-processing module observed in susceptible pigs (An et al., 2024).

Several considerations should be kept in mind when interpreting this study. The core analyses combined spatial transcriptomics with bulk proteomic and N-glycoproteomic profiling and were performed on a limited number of individuals, prioritizing molecular and spatial resolution over population-level inference. While this design enables detailed dissection of tissue-level programs, validation in larger cohorts will be required to assess the robustness and heritability of the identified modules. In addition, our analysis focuses on a single late time point (28 dpi), capturing an established chronic inflammatory state. This design does not resolve the temporal sequence by which interferon attenuation, immune imbalance and structural remodeling emerge, and earlier time points will be essential to distinguish initiating events from downstream consequences. Methodologically, the Visium platform provides multi-cellular rather than single-cell resolution, which may obscure fine-grained heterogeneity within immune compartments and constrain cell–cell communication inference. Although immune deconvolution and targeted validation support the major cellular trends described here, integration with single-cell transcriptomics or higher-plex spatial proteomic approaches will be important to refine cell-type-specific mechanisms. Finally, while our data nominate several pathways of interest, direct functional perturbation will be required to establish causality and to evaluate their translational potential.

In summary, our analyses show that divergent outcomes of Mhp infection arise from differences in immune and tissue organization rather than from differences in bacterial burden. Resistant Yorkshire pigs preserve coordinated interferon signaling, balanced myeloid and lymphoid responses and extracellular matrix programs compatible with barrier maintenance. In contrast, susceptible Chenghua pigs display disrupted interferon and antigen-presentation pathways, humoral-skewed immune amplification and progressive structural remodeling, leading to sustained lung injury despite comparable pathogen load. By resolving these processes in spatial context and integrating them with bulk proteomic and glycoproteomic data, this study helps clarify how host background shapes the integration of inflammatory, cytotoxic and reparative responses in the infected lung, and provides a foundation for future mechanistic, temporal and functional studies of Mhp-associated pneumonia.

DATA AVAILABILITY

Raw spatial transcriptomic sequencing data generated in this study have been deposited in the National Center for Biotechnology Information (NCBI) Gene Expression Omnibus (GEO) under accession number GSE306706, Science Data Bank (DOI: 31253.11.sciencedb.j00139.00ax), and Genome Sequence Archive (GSA, accession No. PRJCA077860). Mass spectrometry-based proteomics data have been deposited in the ProteomeXchange Consortium via the PRIDE partner repository under dataset identifier PXD067630; N-glycoproteomics data are included within this same proteomics dataset.

SUPPLEMENTARY DATA

Supplementary data to this article can be found online.

COMPETING INTERESTS

The authors declare that they have no competing interests.

AUTHORS' CONTRIBUTIONS

Z.J.Z.: data analysis, writing-original draft, writing-review. J.M.C., S.X.Y. and Q.S.: investigation, resources and methodology. P.K.M.T. and D.C.: data curation, methodology and investigation. S.D.C.: software, data curation. R.J.H. and Y.X.Z.: validation and methodology. P.X.W.: investigation and data curation. G.Q.T.: supervision, conceptualization and methodology. All authors have read and approved the final version of this manuscript.

REFERENCES

An Y, Zhu JC, Xie QH, et al. 2024. Tumor exosomal ENPP1 hydrolyzes cGAMP to inhibit cGAS-STING signaling. *Advanced Science*, **11**(20): 2308131.

Ando A, Shigenari A, Kojima-Shibata C, et al. 2016. Association of swine leukocyte antigen class II haplotypes and immune-related traits in a swine line selected for resistance to mycoplasmal pneumonia. *Comparative Immunology, Microbiology and Infectious Diseases*, **48**: 33–40.

Bai FF, Ni B, Liu MJ, et al. 2014. *Mycoplasma hyopneumoniae*-derived lipid-associated membrane proteins induce inflammation and apoptosis in porcine peripheral blood mononuclear cells *in vitro*. *Veterinary Microbiology*, **175**(1): 58–67.

Chae C. 2016. Porcine respiratory disease complex: interaction of vaccination and porcine circovirus type 2, porcine reproductive and respiratory syndrome virus, and *Mycoplasma hyopneumoniae*. *The Veterinary Journal*, **212**: 1–6.

Clough J, Colwill M, Poullis A, et al. 2024. Biomarkers in inflammatory bowel disease: a practical guide. *Therapeutic Advances in Gastroenterology*, **17**: 17562848241251600.

Collignon PJ, McEwen SA. 2019. One health-its importance in helping to better control antimicrobial resistance. *Tropical Medicine and Infectious Disease*, **4**(1): 22.

De Zuani M, Xue HL, Park JS, et al. 2024. Single-cell and spatial transcriptomics analysis of non-small cell lung cancer. *Nature Communications*, **15**(1): 4388.

Deutscher AT, Jenkins C, Minion FC, et al. 2010. Repeat regions R1 and R2 in the P97 paralogue Mhp271 of *Mycoplasma hyopneumoniae* bind heparin, fibronectin and porcine cilia. *Molecular Microbiology*, **78**(2): 444–458.

Deutscher AT, Tacchi JL, Minion FC, et al. 2012. *Mycoplasma hyopneumoniae* surface proteins Mhp385 and Mhp384 bind host cilia and glycosaminoglycans and are endoproteolytically processed by proteases that recognize different cleavage motifs. *Journal of Proteome Research*, **11**(3): 1924–1936.

Dickie R, Tasat DR, Alanis EF, et al. 2009. Age-dependent changes in porcine alveolar macrophage function during the postnatal period of alveolarization. *Developmental & Comparative Immunology*, **33**(2): 145–151.

Drzewicka K, Zasłona Z. 2024. Metabolism-driven glycosylation represents therapeutic opportunities in interstitial lung diseases. *Frontiers in Immunology*, **15**: 1328781.

Fang XM, Zhao WM, Fu YF, et al. 2015. Difference in susceptibility to *Mycoplasma pneumonia* among various pig breeds and its molecular genetic basis. *Scientia Agricultura Sinica*, **48**(14): 2839–2847. (in Chinese)

Feng ZX, Shao GQ, Liu MJ, et al. 2010. Immune responses to the attenuated *Mycoplasma hyopneumoniae* 168 strain vaccine by intrapulmonic immunization in piglets. *Agricultural Sciences in China*, **9**(3): 423–431.

Gan Y, Xie X, Zhang L, et al. 2020. Establishment of a model of *Mycoplasma hyopneumoniae* infection using Bama miniature pigs. *Food Production, Processing and Nutrition*, **2**(1): 19.

Hafemeister C, Satija R. 2019. Normalization and variance stabilization of single-cell RNA-seq data using regularized negative binomial regression. *Genome Biology*, **20**(1): 296.

Holtzman MJ, Byers DE, Alexander-Brett J, et al. 2014. The role of airway epithelial cells and innate immune cells in chronic respiratory disease. *Nature Reviews Immunology*, **14**(10): 686–698.

Huang Y, Zhang HL, Li ZL, et al. 2021. FUT8-mediated aberrant N-glycosylation of B7H3 suppresses the immune response in triple-negative breast cancer. *Nature Communications*, **12**(1): 2672.

Jin SQ, Guerrero-Juarez CF, Zhang LH, et al. 2021. Inference and analysis of cell-cell communication using CellChat. *Nature Communications*, **12**(1): 1088.

Keenan CM, Baker J, Bradley A, et al. 2015. International harmonization of nomenclature and diagnostic criteria (INHAND): progress to date and future plans. *Toxicologic Pathology*, **43**(5): 730–732.

Keir HR, Chalmers JD. 2022. Neutrophil extracellular traps in chronic lung disease: implications for pathogenesis and therapy. *European Respiratory Review: an Official Journal of the European Respiratory Society*, **31**(163): 210241.

Kremer PG, Lampros EA, Blocker AM, et al. 2024. One N-glycan regulates natural killer cell antibody-dependent cell-mediated cytotoxicity and modulates Fc γ receptor IIIa/CD16a structure. *eLife*, **13**: RP100083.

Leal Zimmer FMA, Paes JA, Zaha A, et al. 2020. Pathogenicity & virulence of *Mycoplasma hyopneumoniae*. *Virulence*, **11**(1): 1600–1622.

Lee HS, Qi YF, Im W. 2015. Effects of *N*-glycosylation on protein conformation and dynamics: protein data bank analysis and molecular dynamics simulation study. *Scientific Reports*, **5**: 8926.

Lee JTH, Barnett SN, Roberts K, et al. 2025. Integrated histopathology, spatial and single cell transcriptomics resolve cellular drivers of early and late alveolar damage in COVID-19. *Nature Communications*, **16**(1): 1979.

Li CY, Xue HY, Chen LH, et al. 2025. Identification and validation of glycosylation-related gene signatures for prognostic stratification in sepsis. *Frontiers in Immunology*, **16**: 1608082.

Li HY, Wu M, Zhao X. 2022. Role of chemokine systems in cancer and inflammatory diseases. *MedComm*, **3**(2): e147.

Li JQ, Huang F, Zhou YY, et al. 2024. Comprehensive lung microbial gene and genome catalogs assist the mechanism survey of *Mesomycoplasma hyopneumoniae* strains causing pig lung lesions. *iMeta*, **3**(6): e258.

Liang W, Li ZH, Wang P, et al. 2016. Differences of immune responses between Tongcheng (Chinese local breed) and Large White pigs after artificial infection with highly pathogenic porcine reproductive and respiratory syndrome virus. *Virus Research*, **215**: 84–93.

Lim B, Kim SC, Kim HJ, et al. 2025. Single-cell transcriptomics of bronchoalveolar lavage during PRRSV infection with different virulence. *Nature Communications*, **16**(1): 1112.

Lim KH, Chen LC, Hsu K, et al. 2020. BAFF-driven NLRP3 inflammasome activation in B cells. *Cell Death & Disease*, **11**(9): 820.

Liu MJ, Du GM, Liu B, et al. 2017. Cholesterol exacerbates *Mycoplasma hyopneumoniae*-induced apoptosis via stimulating proliferation and adhesion to porcine alveolar macrophages. *Veterinary Microbiology*, **211**: 112–118.

Liu ZL, Meng XY, Zhang YX, et al. 2024. FUT8-mediated aberrant N-glycosylation of SEMA7A promotes head and neck squamous cell carcinoma progression. *International Journal of Oral Science*, **16**(1): 26.

Maes D, Boyen F, Devriendt B, et al. 2021. Perspectives for improvement of *Mycoplasma hyopneumoniae* vaccines in pigs. *Veterinary Research*, **52**(1): 67.

Maes D, Boyen F, Haesebrouck F, et al. 2020. Antimicrobial treatment of *Mycoplasma hyopneumoniae* infections. *The Veterinary Journal*, **259–260**: 105474.

Maes D, Sibila M, Kuhnert P, et al. 2018. Update on *Mycoplasma hyopneumoniae* infections in pigs: knowledge gaps for improved disease control. *Transboundary and Emerging Diseases*, **65**(S1): 110–124.

Maes D, Verdonck M, Deluyker H, et al. 1996. Enzootic pneumonia in pigs. *Veterinary Quarterly*, **18**(3): 104–109.

Maglione PJ, Gyimesi G, Cols M, et al. 2019. BAFF-driven B cell hyperplasia underlies lung disease in common variable immunodeficiency. *JCI Insight*, **4**(5): e122728.

Mayr CH, Santacruz D, Jarosch S, et al. 2024. Spatial transcriptomic characterization of pathologic niches in IPF. *Science Advances*, **10**(32): eadl5473.

Megas S, Wilbrey-Clark A, Maartens A, et al. 2025. Spatial transcriptomics of the respiratory system. *Annual Review of Physiology*, **87**: 447–470.

Meyns T, Maes D, Calus D, et al. 2007. Interactions of highly and low virulent *Mycoplasma hyopneumoniae* isolates with the respiratory tract of pigs. *Veterinary Microbiology*, **120**(1-2): 87–95.

Mucha SG, Ferrarini MG, Moraga C, et al. 2020. *Mycoplasma hyopneumoniae* J elicits an antioxidant response and decreases the expression of ciliary genes in infected swine epithelial cells. *Scientific Reports*, **10**(1): 13707.

Newman AM, Steen CB, Liu CL, et al. 2019. Determining cell type abundance and expression from bulk tissues with digital cytometry. *Nature Biotechnology*, **37**(7): 773–782.

Ni LG, Song CY, Wu XS, et al. 2019. RNA-seq transcriptome profiling of porcine lung from two pig breeds in response to *Mycoplasma hyopneumoniae* infection. *PeerJ*, **7**: e7900.

Nizamoglu M, Burgess JK. 2021. The Multi-faceted extracellular matrix: unlocking its secrets for understanding the perpetuation of lung fibrosis. *Current Tissue Microenvironment Reports*, **2**(4): 53–71.

Pharmacopoeia E. 2013. Porcine enzootic pneumonia vaccine (inactivated). *In*: European Pharmacopoeia Commission. European Pharmacopoeia. 8th ed. Strasbourg, France: Council of Europe.

Qu MD, Chen ZY, Qiu ZY, et al. 2022. Neutrophil extracellular traps-triggered impaired autophagic flux via METTL3 underlies sepsis-associated acute lung injury. *Cell Death Discovery*, **8**(1): 375.

Reily C, Stewart TJ, Renfrow MB, et al. 2019. Glycosylation in health and disease. *Nature Reviews Nephrology*, **15**(6): 346–366.

Rendeiro AF, Ravichandran H, Bram Y, et al. 2021. The spatial landscape of lung pathology during COVID-19 progression. *Nature*, **593**(7860): 564–569.

Rizo-Téllez SA, Filep JG. 2024. Beyond host defense and tissue injury: the emerging role of neutrophils in tissue repair. *American Journal of Physiology-Cell Physiology*, **326**(3): C661–C683.

Rosales RS, Risco D, García-Nicolás O, et al. 2024. Differential gene expression in porcine lung compartments after experimental infection with *Mycoplasma hyopneumoniae*. *Animals*, **14**(9): 1290.

Saade G, Deblanc C, Bougon J, et al. 2020. Coinfections and their molecular consequences in the porcine respiratory tract. *Veterinary Research*, **51**(1): 80.

Sakuma A, Sugawara S, Hidaka H, et al. 2020. IL-12p40 gene expression in lung and hilar lymph nodes of MPS-resistant pigs. *Animal Science Journal*, **91**(1): e13450.

Sato T, Okamura T, Kojima-Shibata C, et al. 2016. Correlated response of peripheral blood cytokines with selection for reduced *Mycoplasma pneumonia* of swine lesions in Landrace pigs. *Animal Science Journal*, **87**(4): 477–483.

Sha HX, Liu YB, Qiu YL, et al. 2024. Neutrophil extracellular traps trigger alveolar epithelial cell necroptosis through the cGAS-STING pathway during acute lung injury in mice. *International Journal of Biological Sciences*, **20**(12): 4713–4730.

Shimazu T, Borjigin L, Katayama Y, et al. 2014. Genetic selection for resistance to *Mycoplasmal pneumonia* of swine (MPS) in the Landrace line influences the expression of soluble factors in blood after MPS vaccine sensitization. *Animal Science Journal*, **85**(4): 365–373.

Stuart T, Butler A, Hoffman P, et al. 2019. Comprehensive integration of single-cell data. *Cell*, **177**(7): 1888–1902. e21.

Tagore S, Caprio L, Amin AD, et al. 2025. Single-cell and spatial genomic landscape of non-small cell lung cancer brain metastases. *Nature Medicine*, **31**(4): 1351–1363.

Tang Q, Sousa J, Echeverria D, et al. 2022. RNAi-based modulation of IFN-γ signaling in skin. *Molecular Therapy*, **30**(8): 2709–2721.

Tong L, Jiménez-Cortegana C, Tay AHM, et al. 2022. NK cells and solid tumors: therapeutic potential and persisting obstacles. *Molecular Cancer*, **21**(1): 206.

Twaddell SH, Baines KJ, Grainge C, et al. 2019. The emerging role of neutrophil extracellular traps in respiratory disease. *Chest*, **156**(4): 774–782.

Vicente MM, Leite-Gomes E, Pinho SS. 2023. Glycome dynamics in T and B cell development: basic immunological mechanisms and clinical applications. *Trends in Immunology*, **44**(8): 585–597.

Wang HY, Zhang ZZ, Xie X, et al. 2020. Paracellular pathway-mediated *Mycoplasma hyopneumoniae* migration across porcine airway epithelial barrier under air-liquid interface conditions. *Infection and Immunity*, **88**(10): e00470–20.

Wang SN, Böhnert V, Joseph AJ, et al. 2023. ENPP1 is an innate immune checkpoint of the anticancer cGAMP-STING pathway in breast cancer. *Proceedings of the National Academy of Sciences of the United States of America*, **120**(52): e2313693120.

Wang XM, Zhang YY, Wang S, et al. 2022. The role of CXCR3 and its ligands in cancer. *Frontiers in Oncology*, **12**: 1022688.

Wang YF, Gou YW, Yuan R, et al. 2024. A chromosome-level genome of Chenghua pig provides new insights into the domestication and local adaptation of pigs. *International Journal of Biological Macromolecules*, **270**(Pt 1): 131796.

Woolley LK, Fell S, Gonsalves JR, et al. 2012. Evaluation of clinical, histological and immunological changes and qPCR detection of *Mycoplasma hyopneumoniae* in tissues during the early stages of mycoplasmal pneumonia in pigs after experimental challenge with two field isolates. *Veterinary Microbiology*, **161**(1-2): 186–195.

Xu Z, Sun H, Zhang Z, et al. 2020. Selection signature reveals genes associated with susceptibility loci affecting respiratory disease due to pleiotropic and hitchhiking effect in Chinese indigenous pigs. *Asian-Australasian Journal of Animal Sciences (AJAS)*, **33**(2): 187–196.

Yang LY, Liu X, Huang XY, et al. 2022. Integrated proteotranscriptomics reveals differences in molecular immunity between Min and Large White pig breeds. *Biology*, **11**(12): 1708.

Yu YF, Wang J, Han R, et al. 2020. *Mycoplasma hyopneumoniae* evades complement activation by binding to factor H via elongation factor thermo unstable (EF-Tu). *Virulence*, **11**(1): 1059–1074.

Zhang H, Wang YY, Gao L, et al. 2021. Genotype diversity of *Mycoplasma hyopneumoniae* in Chinese swine herds based on multilocus sequence typing. *BMC Veterinary Research*, **17**(1): 347.

Zhang Y, Liu B, Said A, et al. 2023. Regulatory functional role of NLRP3 inflammasome during *Mycoplasma hyopneumoniae* infection in swine. *Journal of Animal Science*, **101**: skad216.

Zhang Z, Xiao Q, Zhang QQ, et al. 2018. Genomic analysis reveals genes affecting distinct phenotypes among different Chinese and western pig breeds. *Scientific Reports*, **8**(1): 13352.

Zhang ZZ, Mei XZ, Wang H, et al. 2025. Long non-coding RNA MMTP mediates necroptosis in alveolar macrophages during *Mycoplasma hyopneumoniae* infection by enhancing TNF-α transcription. *International Journal of Biological Macromolecules*, **288**: 138649.

Zhao X, Jiang L, Fang XY, et al. 2022. Host-microbiota interaction-mediated resistance to inflammatory bowel disease in pigs. *Microbiome*, **10**(1): 115.

Zhou HY, Zhang HL, Zhang XP, et al. 2025. Prevalence and risk factors of *Mycoplasma hyopneumoniae* in swine farms, mainland China, 2003–2024: a meta-analysis. *Veterinary Sciences*, **12**(9): 863.